

A multiple scattering algorithm for three dimensional phase contrast atomic electron tomography

David Ren^{1,*}, Colin Ophus^{1,b}, Michael Chen^a, Laura Waller^a

^a Department of Electrical Engineering and Computer Sciences, University of California, Berkeley, CA 94720, USA

^b NCEM, Molecular Foundry, Lawrence Berkeley National Laboratory, 1 Cyclotron Road, Berkeley, CA 94720, USA

ARTICLE INFO

Keywords:

Transmission electron microscopy
Phase retrieval
Multiple scattering
Optimization
Atomic electron tomography

ABSTRACT

Electron tomography is used in both materials science and structural biology to image features well below the optical resolution limit. Here, we present a new method for high-resolution 3D transmission electron microscopy (TEM) which approximately reconstructs the electrostatic potential of a sample at atomic resolution in all three dimensions. We use phase contrast images captured through-focus and at varying tilt angles, along with an implicit phase retrieval algorithm that accounts for dynamical and strong scattering, providing more accurate results with much lower electron doses than current atomic electron tomography methods. We test our algorithm using simulated images of a synthetic needle geometry dataset composed of an amorphous silicon dioxide shell around a silicon core. By simulating various levels of electron dose, tilt and defocus, missing projections, and regularization methods, we identify a configuration that allows us to accurately determine both atomic positions and species. We also test the ability of our method to recover randomly positioned vacancies in light elements such as silicon, and to accurately reconstruct strongly-scattering elements such as tungsten.

1. Introduction

Transmission electron microscopy (TEM) offers unprecedented resolution for imaging applications in biology and materials science [1,2]. Modern systems can quantitatively reconstruct 3D local structure, electrostatic and magnetic potentials, and local chemistry [3]. Recent progress enables locating the 3D position of individual atoms with high precision [4–6], and even determining both the 3D position and species of every atom in a nanoscale sample [7]. These atomic electron tomography (AET) studies use a TEM imaging mode called annular dark field (ADF) scanning transmission electron microscopy (STEM). ADF-STEM generates contrast that increases monotonically with the 2D projection of the 3D electrostatic potential of the sample along the beam direction. Such approximated linearity allows for traditional tomographic reconstruction algorithms [8,9]. However, ADF-STEM requires large electron doses, as it is much less efficient than phase contrast imaging [10,11]. Additionally, because the electron probe is focused to a small spot and scanned over the sample surface, sample motion during the experiment can cause artifacts [12].

The simplest phase contrast imaging mode used in TEM studies is plane-wave illumination, usually referred to as high-resolution transmission electron microscopy (HRTEM). However, at atomic resolution,

HRTEM imaging produces highly nonlinear contrast for any sample thicker than a few atomic monolayers, making it difficult to interpret the results [13,14]. For thin samples, comparing experiments to simulations can recover some quantitative 3D information [15,16], but this is difficult or impossible for experiments with a high degree of multiple electron scattering. Thus, phase contrast imaging is not widely used in materials science electron tomography studies at atomic resolution.

By comparison, phase contrast HRTEM imaging in biology is simpler to interpret because most biological specimens can be approximated as *weak phase objects*, allowing for the sample's phase to be reconstructed from a single defocused intensity measurement [17]. This single-image requirement is important for biological samples because they tend to be extremely sensitive to electron beam damage and cannot tolerate the much higher electron doses used in materials science [18]. In structural biology, the introduction of direct electron detectors with high quantum efficiency [19] has rapidly expanded the number of solved protein structures, using 3D tomographic averaging of images of many identical or near-identical protein structures with random orientations. This technique is called single particle cryo-electron microscopy (cryo-EM) [20]. When imaging larger biological samples, averaging of sub-volumes can also produce high-resolution reconstructions [21].

Recent advances in computational methods have improved

* Corresponding author.

E-mail addresses: david.ren@berkeley.edu (D. Ren), cophus@gmail.com (C. Ophus).

¹ These two authors contributed equally.

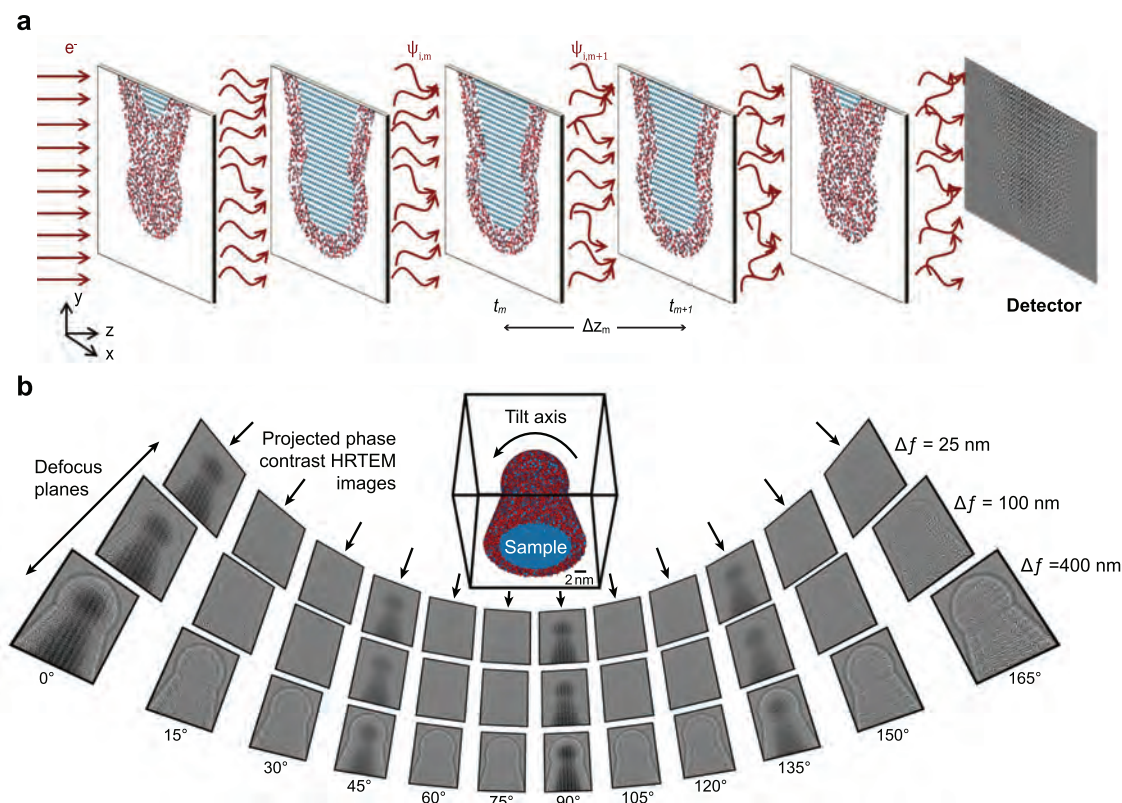


Fig. 1. Experimental setup for phase contrast atomic electron tomography experiment with a core-shell SiO₂ needle geometry. (a) The multislice forward model treats the 3D sample as a series of 2D slices separated by propagation, thus accounting for multiple scattering. (b) The sample is tilted with respect to the electron beam to capture plane-wave illuminated images at varying angles (up to 180°). For each tilt angle several HRTEM images are recorded at different focus planes.

reconstruction accuracy even further, for example by introducing a correction for the microscope contrast transfer function (CTF) [22]. However, advanced algorithms generally make a weak object assumption and treat the measured signal as a linear sum of the projected potential [23]. This linearizes the physical model in order to provide a closed-form solution, but these assumptions usually only hold for very thin samples [24]. Nonlinear effects of multiple scattering are non-negligible for thick samples, which represent a large majority of materials science samples. Therefore, thick samples require both a nonlinear forward model and a reconstruction method that captures the dynamical scattering of the electron beam.

Nonlinear phase reconstruction in 2D for TEM includes algorithms for reconstruction of the sample potential phase contrast measurements [25,26], maximum likelihood methods [27–29], and other iterative algorithms [30–33]. These methods, however, are usually limited to samples that are either single scattering or satisfy crystal approximations.

Methods to correct for multiple scattering in 3D phase reconstructions have been proposed in optics [34–41]. A typical strategy - the multislice or beam propagation method [14,42,43] - treats the 3D object as a series of 2D slices, each with its own transmittance function, separated by small distances of free-space propagation. For TEM, the interaction of the electron beam with the sample can thus be modeled by two linear operators. The first is a multiplication by the transmittance function that describes the absorption and phase delay of the electron beam when interacting with that slice of the sample. The second is the free space propagation operator, which captures the dynamics of propagation. Unfortunately, these two operators do not commute, making the inverse scattering calculation both nonlinear and non-convex. Van den Broek and Koch have proposed an inversion method for multiple electron scattering, which uses multiple beam tilt

projections for phase contrast TEM imaging to perform a 3D reconstruction with very few layers [43–45] similar to 3D Fourier Ptychographic Microscopy [41]. In simulation, they were able to reconstruct the atomic potential of a small nanoparticle in 3D from a small number of tilt angles, for strongly scattering atoms and a low TEM accelerating voltage of 40 kV, and assuming structural priors. However, the 3D transfer function for tilting the beam results in non-isotropic resolution [46,47]; hence, the axial resolution is fundamentally limited when assuming no structural priors on the sample.

In this paper, we present an isotropic atomic-resolution method for 3D reconstruction from intensity-only images taken at varying tilt angles and defocus values. Our algorithm models multiple scattering of the electron beam and strong phase shifts induced by individual atoms. Further, we introduce an efficient regularization scheme that exploits the well-known structure of atoms in order to obtain a physically-accurate result, even with very low signal-to-noise ratio (SNR). After reconstruction, we use an atom-tracing algorithm that is capable of identifying individual atoms as well as estimating their sub-voxel 3D positions and chemical species. Our proposed method will allow AET experiments to be performed on samples that contain weakly scattering elements such as carbon, oxygen or even lithium, with either crystalline or amorphous structures, or a mix of both. Taken together, these improvements enable imaging of thicker samples and those that cannot withstand high electron doses. Biological cryo-EM studies may also benefit if they are performed on very large volumes (where the projection assumption breaks down) or contain multiple scattering regions. Assuming a biological tomography experiment had a dose-limited resolution of approximately 1 nm, the reconstruction size used in this study with a voxel size of 0.5 nm could reconstruct a volume of (240 nm)³.

2. Methods

2.1. Atomic structure of the sample

We consider a two-component sample structure, with a tip geometry similar to the experiment described in [6] (and shown in Fig. 1). The structure consists of a crystalline silicon core and a silicon dioxide outer layer. The crystalline core has a tip diameter of approximately 10 nm, as in experiments [48]. A 2 nm thick shell of SiO₂ surrounds the entire Si tip. The SiO₂ coordinates were taken from the SiO₂ structure given in [49], which were computed using Density Functional Theory (DFT). Additionally, a 1.2 Å minimum distance was enforced between the atomic positions of the Si core and SiO₂ shell. In total, 150,847 atoms are present in the structure.

The overall structure of this sample is complex. It contains both fully crystalline and fully amorphous regions along the beam direction for all projection directions. Also, while silicon scatters the electron beam with a moderate cross-section, oxygen atoms scatter only weakly. Finally, the amorphous SiO₂ structure has an Si-O bond length of approximately 1.6 Å [50], making it challenging to resolve the individual atoms in this structure. Hence, this is a challenging test object with realistic length scales for AET reconstruction algorithms.

2.2. Simulation setup & parameters

Data is captured using the simplest TEM measurement protocol: plane-wave illumination, typically referred to as HRTEM or phase contrast imaging. Using a modern TEM instrument equipped with hardware aberration correction, we can image the sample with very little aberrations and sufficient coherence for atomic resolution imaging [51,52]. Fig. 1(b) shows examples of simulated HRTEM plane-wave images.

To capture phase information, we use through-focus HRTEM images at each tilt (rotation) angle. Defocusing the electron wave increases contrast and delocalizes the atomic signal (see Fig. 1(b)). In this near-field, or Fresnel diffraction regime, each image is high-pass filtered by the microscope, and the measured signal is modulated by the CTF [14], which can lead to spatial frequency pass-bands or contrast inversions.

The sample is mounted on a tilt-rotation stage so that it can be rotated with respect to the electron beam. For the tip sample considered here, a full tilt range of 180° has been demonstrated [6] with the TEAM stage [53]. However, most electron tomography experiments have a “missing wedge” of tilt angles where the sample geometry or stage prevent measurements at some projection angles. Therefore, we consider both the full-angle and the missing wedge situations. When the tilt direction is closely aligned with the crystalline silicon region of the sample (the low-index zone axis imaging conditions), strong image contrast is observed (Fig. 1(b)).

In the meantime, we choose parameters that can be realistically achieved in experiments:

Electron energy: In order to achieve very high resolution, we use an electron accelerating voltage of 300 kV (de Broglie wavelength 0.0197 Å), as in [6,7]. While SiO₂ is known to be sensitive to the electron beam, it has been imaged previously using 300 kV HRTEM [54–57].

Voxel size: The voxel size of 0.5 Å (isotropic in all three dimensions) gives a good balance between resolution and field-of-view (FoV), with consideration for practical limits on computation. This voxel size can resolve individual atoms in the amorphous SiO₂ structure (average Si-O bond length of 1.6 Å). Our reconstruction volume is computationally limited to (24nm)³, corresponding to 480³ = 1.1·10⁸ voxels, which requires 422 MB of storage space for each full array at single floating point precision. Because we operate in complex space, the storage size requirements double to 844 MB. Without loss of generality, our final reconstruction volume contains a large majority of the sample, which

includes approximately 120,000 atoms. In the appendix we show that this voxel size is sufficient by reconstructing from measurements generated with a much smaller voxel size of 0.1 Å.

Tilt angles: Due to the nonlinearity of multiple scattering, choosing the optimal set of tilt angles analytically is not possible. However, we can get a good estimate by using a linear approximation (single scattering) from optical diffraction tomography [47,58], which treats each tomographic measurement as coming from a particular subspace of the sample’s 3D Fourier spectrum (specifically, a parameterized 2D surface). Crystalline samples have distinct preferred measurement directions, but amorphous materials do not [59]. Since our sample contains both, we choose tilt angles that are equally spaced, in order to evenly span Fourier space. In simulations, we mimic experimental limitations by simulating the effect of a missing wedge where some range of tilt angles are missing.

Defocus: As few as two measurements taken at different focus positions can provide phase information [60]. More images will improve the phase result, but must be traded off against dose, data size and capture time. Linearly-spaced focus steps have been shown to be an inefficient scheme for capturing all spatial frequencies; instead, we use exponentially-spaced focus steps [61]. Positive and negative defocus provide essentially identical information about the sample (up to a sign difference) for aberration-corrected microscopes, so we defocus the electron wave in one direction only. As a practical issue, we further restrict the defocus to small enough magnitudes to enable easy translation alignment of multiple images. Due to the increased signal delocalization, large defocus values also require a larger FoV and correction of any magnification or rotation errors, which would increase complexity.

2.3. Forward simulation

First, we describe our computational model for the process of the incident beam interacting with the sample and forming each measurement; this *forward model* is used to simulate measurements and will also be crucial to our inverse problem reconstruction. It is composed of three parts: object rotation, complex-wave propagation and imaging. We model the 3D object as a series of projected 2D atomic potential functions $V \triangleq \{V_m(\mathbf{r})\}_{m=1}^{N_z}$, where $\mathbf{r} = (x, y)$ are the lateral coordinates and m is the slice index along the axial direction (z) [14], with slice separation described by a set $\{\Delta z_m\}_{m=1}^{N_z}$.

For each tilt angle, θ_k ($k = 1, 2, \dots, N_\theta$), we rotate the 3D object along the y -axis using a fast rotation algorithm [62]. The tilted object W_k is then $W_k = \mathcal{R}_{\theta_k}\{V\}$, where \mathcal{R}_{θ_k} denotes a linear rotation operator.

Then, we model the propagation of the complex wave, with relativistically-corrected electron wavelength λ , through the object. We use a multislice algorithm to account for multiple scattering events (see Fig. 1(a)). Each slice is converted from a 2D potential function to a 2D transmittance function $t_{k,m}(\mathbf{r}) = \exp[i\sigma W_{k,m}(\mathbf{r})]$, where σ is the beam-sample interaction parameter that depends linearly on λ . Example projected potentials are shown in Fig. 2(b) and (c).

The complex electron wave function before reaching each slice is denoted by $\psi_{k,m}(\mathbf{r})$. As it passes through the slice, it will be multiplied by the corresponding 2D transmittance function at the corresponding z depth. After that, it is propagated in free space to the next slice using the angular spectrum method:

$$\psi_{k,m+1}(\mathbf{r}) = \mathcal{P}_{\Delta z_m}\{t_{k,m}(\mathbf{r})\psi_{k,m}(\mathbf{r})\}, \quad (1)$$

where

$$\mathcal{P}_{\Delta z_m}\{\cdot\} = \mathcal{F}^{-1}\{\exp[i2\pi\Delta z_m\sqrt{1/\lambda^2 - \|\mathbf{q}\|^2}]\cdot\mathcal{F}\{\cdot\}\} \quad (2)$$

is the linear operator for free-space propagation by distance Δz_m , $\mathbf{q} = (q_x, q_y)$ is the 2D Fourier space coordinates, and $\mathcal{F}\{\cdot\}$ and $\mathcal{F}^{-1}\{\cdot\}$ denote Fourier transform and its inverse, respectively.

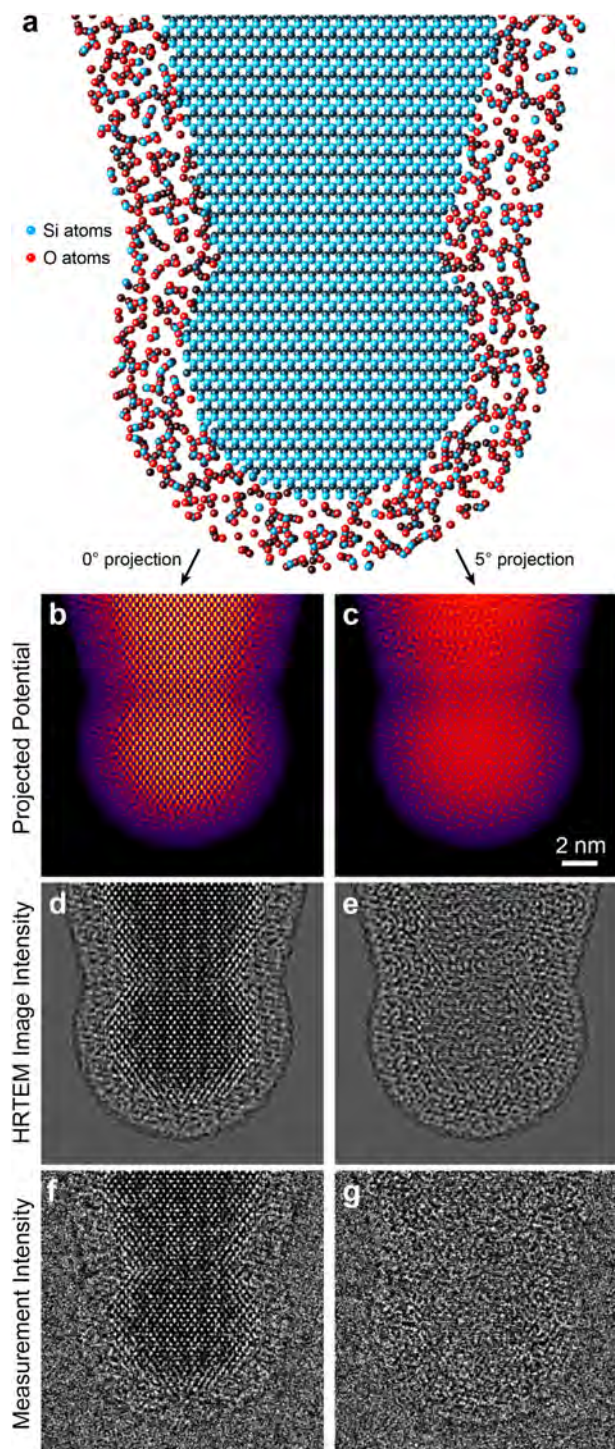


Fig. 2. HRTEM simulation of the SiO_2 model. (a) A slice of the atomic structure, perpendicular to the electron beam direction. (b) The summed 2D projected potential of the object at 0° and (c) 5° rotation, with intensity scaled to show the weakly scattering edges. (d),(e) Noise-free (infinite dose) HRTEM images at 100 nm defocus for (b) and (c), respectively. (f),(g) Noisy versions of the same images, simulating a dose of 40 electrons/ \AA^2 .

The exit wave of a thin sample (in focus) will show primarily amplitude contrast, but most of the electron scattering information is encoded as phase shifts on the exit wave. Because defocus induces phase contrast, we use the free-space propagation operator to defocus the exit waves by distances of $\{\Delta f_j\}_{j=1}^{N_f}$ before capturing the intensity of the exit wave:

Input: Initial wave function $\psi_0(\mathbf{r})$, 3D rotated atomic potentials $W = \{W_m\}_{m=1}^{N_z}$, slice separations $\{\Delta z_m\}_{m=1}^{N_z}$, defocus angles $\{\Delta f_j\}_{j=1}^{N_f}$, and interaction parameter σ .

- 1: $\psi_1(\mathbf{r}) \leftarrow \psi_0(\mathbf{r})$
- 2: **for** $m \leftarrow 1$ to N_z **do**
- 3: $t_m(\mathbf{r}) \leftarrow \exp[i\sigma W_m(\mathbf{r})]$
- 4: $\psi_{m+1}(\mathbf{r}) \leftarrow \mathcal{P}_{\Delta z_m}\{t_m(\mathbf{r}) \cdot \psi_m(\mathbf{r})\}$
- 5: **end for**
- 6: **for** $j \leftarrow 1$ to N_f **do**
- 7: $\psi_{\text{exit},j}(\mathbf{r}) \leftarrow \mathcal{H}\{\mathcal{P}_{\Delta f_j}\{\psi_{N_z+1}(\mathbf{r})\}\}$
- 8: **end for**

Return: Predicted exit wave $\{\psi_{\text{exit},j}(\mathbf{r})\}_{j=1}^{N_f}$ and intermediate wave function $\{\psi_m(\mathbf{r})\}_{m=1}^{N_z}$.

Algorithm 1. Forward model computation.

▷ Beam propagation

▷ Defocus and image

$$\hat{I}_{k,j}(\mathbf{r}) = \left| \mathcal{H} \left\{ \mathcal{P}_{\Delta f_j} \{ \psi_{k,N_z+1}(\mathbf{r}) \} \right\} \right|^2 \triangleq |\psi_{\text{exit},k,j}(\mathbf{r})|^2, \quad (3)$$

where

$$\mathcal{H}\{\cdot\} = \mathcal{F}^{-1}\{H(\mathbf{q}) \cdot \mathcal{F}\{\cdot\}\}, \quad (4)$$

with $H(\mathbf{q})$ denoting the microscope's transfer function [14]. After all tilt angles and defocus images are acquired, we obtain a series of images $\{\hat{I}_{k,j}(\mathbf{r})\}_{k=1,j=1}^{N_g, N_f}$, examples of which are shown in Fig. 2(d) and (e). The multislice beam propagation method is outlined in Algorithm 1 and schematics are shown in Fig. 1(a).

To image the sample with minimal damage, a low dose is required, resulting in noisy measurements. The noise can be modeled by an electron counting process, with each pixel incurring Poisson noise with mean $\{\hat{I}_{k,j}(\mathbf{r})\}_{k=1,j=1}^{N_g, N_f}$. Fig. 2(f) and (g) illustrate a measurement process with a total electron budget of 7000 electrons/ \AA^2 , which is equivalent to approximately 40 electrons/ \AA^2 when distributed across 60 tilt angles having 3 defocused images each.

2.4. Reconstruction algorithm

Given a set of intensity-only measurements, we estimate the potential, V , by solving an optimization problem. Starting with an estimated potential V , we use our forward model to generate a series of predicted measurements $\{\hat{I}_{k,j}(\mathbf{r})\}_{k=1,j=1}^{N_g, N_f}$. We formulate an error function to quantify the difference between predicted and actual measurements $\{I_{k,j}(\mathbf{r})\}_{k=1,j=1}^{N_g, N_f}$. The goal is to find the 3D atomic potential that fits the intensity measured and thus minimizes the error:

$$\begin{aligned} V &= \arg \min_V \sum_{k=1}^{N_g} \sum_{j=1}^{N_f} e_{k,j}^2 \\ &= \arg \min_V \sum_{k=1}^{N_g} \sum_{j=1}^{N_f} \left\| \sqrt{I_{k,j}(\mathbf{r})} - \sqrt{\hat{I}_{k,j}(\mathbf{r})} \right\|_2^2, \end{aligned} \quad (5)$$

where $\|\cdot\|_2$ is the l_2 norm. Instead of directly comparing the difference between the predicted and actual intensity measurements, we compare the square roots of the intensity, which correspond to the amplitude of the exit waves. This is because the amplitude-based error function better accounts for Poisson-distributed noise (whereas an intensity-based error function would be ideal for Gaussian-distributed noise) [63]. In this study, the low electron dose means that Poisson noise dominates.

We solve the optimization problem with an accelerated gradient method outlined in Algorithm 3. For each tilt angle and defocus, we first tilt the estimated sample and predict the intensity using the

Input: Residual vectors $\{r_j(\mathbf{r})\}_{j=1}^{N_f}$, intermediate wave functions $\{\psi_m(\mathbf{r})\}_{m=1}^{N_z}$, 3D rotated atomic potentials W , slice separations $\{\Delta z_m\}_{m=1}^{N_z}$, defocus angles $\{\Delta f_j\}_{j=1}^{N_f}$, and interaction parameter σ .

- 1: $\phi_{N_z+1}(\mathbf{r}) \leftarrow 0$
- 2: **for** $j \leftarrow 1$ to N_f **do** ▷ Refocus to end of sample
- 3: $\phi_{N_z+1}(\mathbf{r}) \leftarrow \phi_{N_z+1}(\mathbf{r}) + \mathcal{P}_{-\Delta f_j} \{ \mathcal{H}^\dagger \{ r_j(\mathbf{r}) \} \}$
- 4: **end for**
- 5: **for** $m \leftarrow N_z$ to 1 **do** ▷ Backpropagation
- 6: $\phi_m(\mathbf{r}) \leftarrow \mathcal{P}_{-\Delta z_m} \{ \phi_{m+1}(\mathbf{r}) \}$
- 7: $t_m^*(\mathbf{r}) \leftarrow \exp[-i\sigma W_m(\mathbf{r})]$
- 8: $g_m(\mathbf{r}) \leftarrow -i\sigma t_m^*(\mathbf{r}) \cdot \psi_m^*(\mathbf{r}) \cdot \phi_m(\mathbf{r})$
- 9: $\phi_m(\mathbf{r}) \leftarrow t_m^*(\mathbf{r}) \cdot \phi_m(\mathbf{r})$
- 10: **end for**

Return: Estimated gradient $\nabla_w e_i \triangleq \{g_m(\mathbf{r})\}_{m=1}^{N_z}$.

Algorithm 2. Error backpropagation for gradient computation.

multislice algorithm outlined in Algorithm 1. Next, we minimize Eq. (5) by differentiating the error with respect to each slice of V . This is done by recursively applying the chain rule to calculate the gradient, and we refer to this process as the backpropagation. The back propagation is illustrated in Algorithm 2, and it is derived in the appendix. Notice that the symmetry between Algorithms 1 and 2 is a key signature in many non-linear optimization methods. Then, we perform a regularization process that enforces prior knowledge we have about the sample (details discussed later). The last step in the loop is that we apply Nesterov's acceleration, which adds a momentum factor in the gradient update to improve convergence speed. By repeating these steps, we finally reach a converged estimate of V and terminate Algorithm 3. Notice that the reconstruction algorithm implicitly solves the phase retrieval problem in the gradient calculation. Line 7 of Algorithm 3 closely resembles the traditional Gerchberg-Saxton type phase retrieval method by applying an amplitude substitution to the residual error [64].

Algorithms that assume lattice types and occupancies inevitably preclude detection of small scale spatial variations. Notice that during the reconstruction, we do not assume any structural priors on the sample. Thus, our method is robust enough to show vacancies and defects when they are present in the sample. In contrast to Van den Broek and Koch [43,44], we also do not assume specific shapes of the individual atoms.

2.5. Regularization

Although the objective function in Eq. (5) accounts for Poisson-distributed noise, the reconstruction quality will still suffer with increased noise. In addition, as we lower the number of measurements, the inverse problem becomes more ill-posed. We use a regularization scheme to incorporate *a priori* knowledge that can mitigate this problem. The regularized cost function is:

$$V = \arg \min_V \left\{ \sum_{k=1}^{N_g} \sum_{j=1}^{N_f} e_{k,j}^2 + \tau R(V) \right\}, \quad (6)$$

where $R(\cdot)$ is a general penalty function, and τ is a tuning parameter for the strength of regularization.

We tested several common types of regularization methods. LASSO (also known as l_1) regularization, where $R(V) = \|V\|_1$, promotes sparsity in the natural domain and is extensively used in statistical parameter estimations [65]. Total Variation (TV) regularization [66], where $R(V) = \|\mathcal{D}\{V\}\|_1$, with $\mathcal{D}\{\cdot\}$ denoting the finite difference operator, is a well-known denoising technique. TV enforces piece-wise smoothness between neighboring pixels by promoting sparsity in the finite difference domain. Since we know that the 3D atomic potential is a smoothly

Input: Tilt angles $\{\theta_k\}_{k=1}^{N_\theta}$, measured intensity images $\{I_{k,j}\}_{k=1,j=1}^{N_\theta,N_f}$, interaction parameter σ , step size α , and maximum iteration N_s .

- 1: $U^{(1)} \leftarrow 0, V^{(0)} \leftarrow 0, \beta^{(1)} = 1$
- 2: **for** $s \leftarrow 1$ to N_s **do** ▷ Outer loop
- 3: **for** $k \leftarrow 1$ to N_θ **do** ▷ Object rotation
- 4: $W_k = \mathcal{B}_{N_B} \{ \mathcal{R}_{\theta_k} [U^{(s)}] \}$
- 5: $(\{\psi_{\text{exit},k,j}\}_{j=1}^{N_f}, \{\psi_{k,m}\}_{m=1}^{N_z}) \leftarrow \text{run Algorithm 1 with } W_k$
- 6: **for** $j \leftarrow 1$ to N_f **do** ▷ Compute residual
- 7: $r_{k,j} \leftarrow \psi_{\text{exit},k,j} - \sqrt{I_{k,j}} \frac{\psi_{\text{exit},k,j}}{|\psi_{\text{exit},k,j}|}$
- 8: **end for**
- 9: $\nabla_W e_k(U^{(s)}) \leftarrow \text{run Algorithm 2 with } \{r_{k,j}\}_{j=1}^{N_f}, \{\psi_{k,m}\}_{m=1}^{N_z}, \text{ and } W_k$
- 10: $U^{(s)} \leftarrow U^{(s)} - \alpha \mathcal{R}_{\theta_k}^\dagger \{ \mathcal{B}_{N_B}^\dagger [\nabla_W e_k(U^{(s)})] \}$
- 11: **end for**
- 12: $V^{(s)} \leftarrow \text{prox}(U^{(s)})$ ▷ Regularization
- 13: $\beta^{(s+1)} \leftarrow \frac{1 + \sqrt{1 + 4(\beta^{(s)})^2}}{2}$ ▷ Nesterov acceleration
- 14: $U^{(s+1)} \leftarrow V^{(s)} + \left(\frac{\beta^{(s)} - 1}{\beta^{(s+1)}} \right) (V^{(s)} - V^{(s-1)})$
- 15: **end for**

Return: Estimated atomic potential $V^{(s)}$.

Algorithm 3. Iterative reconstruction.

varying function, we choose to implement TV regularization here.

We use a proximal gradient implementation, outlined in [Algorithm 3](#). First, we compute the gradient sequentially using through-focus intensities captured at different angles. Then, we evaluate the proximal operator of the regularization techniques. LASSO regularization has an efficient closed-form evaluation; however, the evaluation for the TV proximal operator is in itself another iterative algorithm [67]. In addition, since we assume in simulation that the atomic potential is purely real and positive (i.e. no absorption of the electron beam), we use a positivity constraint to refine our solution space, enforced by performing a projection of the estimate onto real and positive space. In the case where absorption is present, we can remove the constraint without changing the algorithm.

2.6. Measurements of atom positions and species

After using the algorithm described above to reconstruct the atomic potentials, the final step is to use the depth or size of the atomic potential wells to estimate the atomic coordinate positions and classify the atomic species. We have adopted a similar atomic refinement strategy as previous AET studies [6,7], which is referred to as ‘‘atom tracing.’’ First, the reconstructed volume is filtered with a smoothing kernel - a 3D Gaussian distribution with a standard deviation of 0.5 voxels minus another Gaussian distribution with a standard deviation of 1 voxel, normalized to zero total amplitude. Next, the local maxima are recorded as candidate atomic sites. These site positions are refined by fitting a 3D Gaussian function using nonlinear least squares. Next, the fitted intensities are subtracted from the reconstructed volume and candidate atomic sites are added by again filtering with a smoothing kernel and finding local maximum.

Next, an iterative fitting routine proceeds; for each atomic candidate, the nearest-neighbor site intensities are subtracted from the reconstructed volume. In this subtracted volume, nonlinear least squares is used to refine the 3D Gaussian function. After each of these iterations, several criteria were used to remove atomic coordinates. Any sites with a very low intensity (below 30 V, approximately 10% of the maximum sample potential) or size below 1 voxel were removed, and any sites within 2.25 voxels of another site were merged into a single site. After approximately 12 refinement steps, each reconstruction trial was removing less than 2 atomic sites per iteration, and the root-mean square

(RMS) change in atomic positions was less than 0.005 voxels. Note that the thresholds were chosen to give good average performance across all datasets, and were not changed except in one specific instance described below.

To classify atom species, we first generate a histogram of atom intensities. We then fit the histogram curve with a bi-modal Gaussian distribution and choose the intersection of the two Gaussian distributions to be the species classification threshold. All atoms having intensities less than the threshold will be classified as oxygen, and the rest will be classified as silicon.

While the full reconstructed volume contains over 120,000 atoms, we select a smaller volume containing 62,402 atom sites to compare with the ground truth atomic configuration, in order to demonstrate accuracy in atom-tracing and atom identification.

3. Results and discussion

The following sections show the results of varying several experimental or reconstruction parameters. For each, we show a single slice of the normalized reconstructed atomic potential that is perpendicular to the tilt axis. The slice was taken from the thickest part of the protrusion, where the diameter is approximately 12 nm. We plot the atomic coordinates that were correctly found for each slice, and the missing and false positives.

Additionally, we show tetrahedral shapes for each cluster of 5 atoms that formed a tetrahedron, with bond lengths of the 4 corner atoms to the center atom within 0.375 Å of the mean Si-O bond length of 1.6 Å. These tetrahedra help visualize how well the amorphous region of the sample was reconstructed, especially for reconstructions with a lot of noise or artifacts present. This feature classification is an example of the kind of classification measurement that could be performed even in the absence of clear atomic peaks, as is done in structural biology [68].

Next, we show two histograms that quantify how well we trace the individual atoms in [Fig. 4](#). The first histogram shows the statistics of the atomic potential intensities of identified atoms. The more resolved the two distributions are, the better we have classified the specific types of the atoms. The second histogram shows the errors of the 3D position estimation from the reconstruction. Here, for each identified atom we adopt the root-mean-square (RMS) from all coordinates:

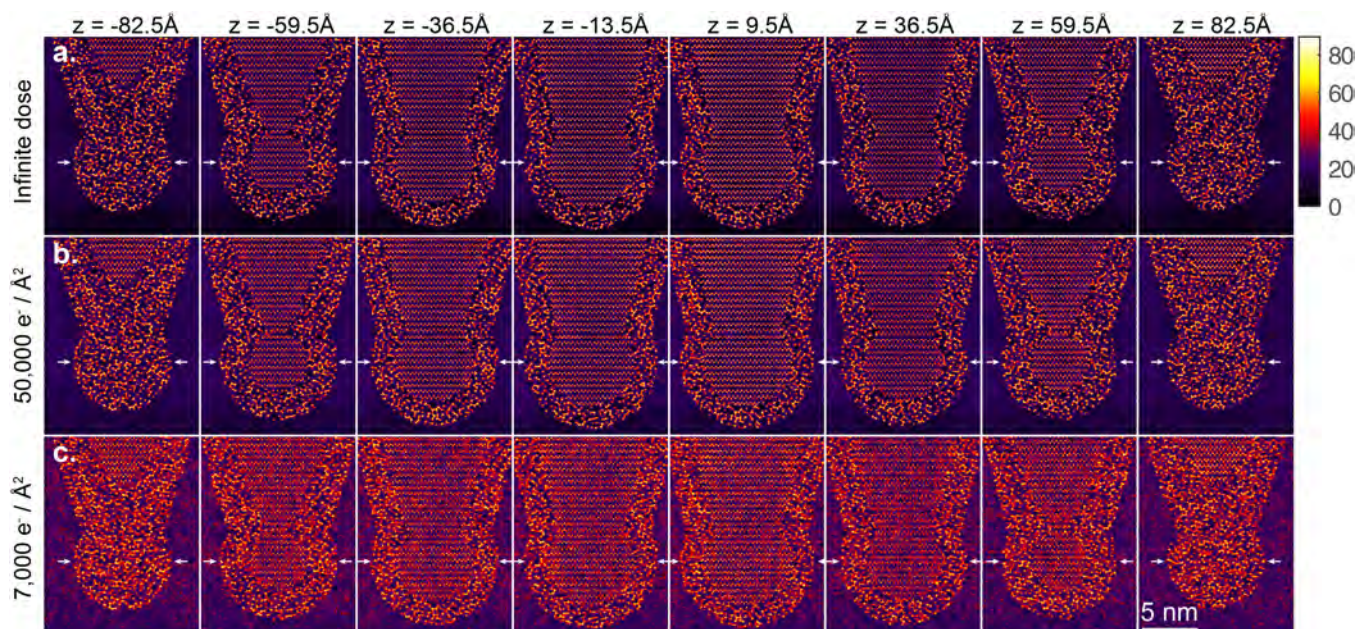


Fig. 3. Varying dose. Phase contrast AET reconstructions of 1 Å thick 2D atomic potential slices of a simulated Si-SiO₂ reconstruction in $x - y$ across multiple z depths, using 60 tilt angles and 3 defocus values per angle. (a) Infinite dose (no noise), (b) 50,000 electrons/Å², and (c) 7000 electrons/Å² total dose. Lower dose results in more noise, which causes errors and artifacts in the reconstruction. Each slice shows the square root of the reconstructed potential from 0 to 80 V and the tilt axis is along the vertical direction. White arrows show location of reconstruction slices for the following sections in Fig. 4.

$$\text{Position Error} = \sqrt{(x^* - \hat{x})^2 + (y^* - \hat{y})^2 + (z^* - \hat{z})^2}, \quad (7)$$

where x^* , y^* , z^* are the true coordinates and \hat{x} , \hat{y} , \hat{z} are the estimated coordinates. A good reconstruction's histogram has a peak close to 0 and a narrow main lobe. We also show RMS error (e) in all three dimensions.

All reconstructions, unless otherwise stated, are full-angle TV regularized, created from 60 uniformly spaced tilt angles, each with 3 defocus steps (25, 45, 100nm) with total incident electron count of 50,000 electrons/Å². The regularization parameter τ in Eq. (6) is chosen such that the background noise is suppressed, without over-smoothing (smearing) the adjacent atoms.

Reconstructions are computed on graphics processing unit (GPU) for accelerated computation (12GB NVIDIA Titan X GPU) and the algorithm converges within 40 iterations for all scenarios. The total computation time for the dataset mentioned above is less than 2 hours.

3.1. Effect of electron dose

In the first set of simulations, reconstructions using different dose budgets are compared to examine how noise affects the algorithm performance. We chose three doses: infinite (noiseless), 50,000 electrons/Å², and 7000 electrons/Å². Fig. 3(a)-(c) shows lateral slices at multiple z depths, taken from simulations with different dose levels. Fig. 4 shows a 1 Å thick $z - x$ cross-section slice (intensity normalized), where the location is indicated by the white arrows in Fig. 3, and atom tracing results. In all reconstructions, the atomic peaks are easily identified. The reconstruction using 50,000 electrons/Å² total dose over all tilts and defocused images is nearly identical to the infinite dose reconstruction.

As expected, the reconstruction quality eventually deteriorates as we decrease the dose budget, with the background becoming noticeably more noisy. We cannot increase the regularization to compensate, as it will over-smooth the reconstruction. For the dose level of 7000 electrons/Å², atoms that are too close to each other are smeared together and missing sites increase. Noisy fluctuations in the background lead to an increased number of false positive sites. The noise also causes loss of

contrast in the atomic potential intensity, which can be seen from the intensity histogram; the distributions of two types of atoms are less resolved when dose is decreased, making it harder to classify the species of individual atoms. Finally, the RMS position estimation error increases isotropically as we decrease the dose level.

Fig. 5 shows the example plots of cost function (Eq. (5)) vs iterations. Despite the convergence, as we lower the dose budget, the predicted intensity of the reconstruction has more mismatch with the measured intensity, causing the squared error to increase.

3.2. Effect of number of tilt and defocus measurements

Because total dose is distributed across measurements from all tilt angles and defocus distances, we face a trade-off between number of tilt angles (N_θ) and number of defocus planes (N_f). In this set of simulations, we compare the performance of our method as we vary N_θ and N_f , while keeping the total dose level constant (50,000 electrons/Å²). Fig. 6 shows reconstructions from three scenarios: 20 tilt angles (separated by 9°) with 9 defocus planes (20 nm-100 nm in steps of 10 nm), 60 tilt angles with 3 defocus planes (20 nm, 45 nm, and 100 nm), and 180 tilt angles with a single plane at 100 nm. These values give a good balance between using larger defocus values to produce more contrast, but not large enough to make image alignment difficult or lose resolution due to coherence limits.

Comparing Fig. 6(a) and (b), we find that using fewer defocus planes and more tilt angles results in a better reconstruction of the sample's structure and improved atom tracing. Particularly in the amorphous SiO₂ region, the number of missing sites is greatly reduced by using more tilt angles. Given that phase can be recovered from a few defocus planes [61], it is reasonable that 9 focus steps are not necessary. However, more focus steps should help to better reconstruct the atomic potential [61]. For the case of only one defocus plane (Fig. 6(c)), the site intensity histograms show that the distributions of the silicon and oxygen atoms are not as well resolved. Hence, the case in Fig. 6(b) gives a good tradeoff between accurate structure recovery and good atom classification.

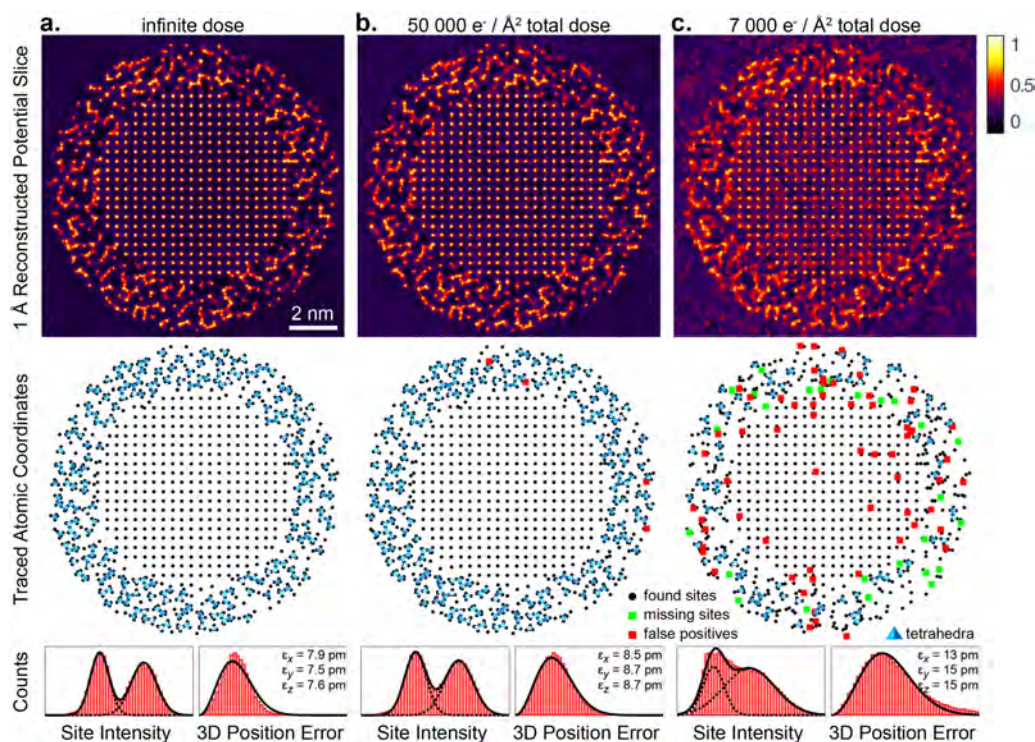


Fig. 4. Varying dose. Phase contrast AET reconstructions in $z - y$ direction for (a) infinite electron dose, (b) 50,000 electrons/ \AA^2 , and (c) 7000 electrons/ \AA^2 total dose. We show (top row) a slice of the normalized reconstructed potential and (bottom row) the corresponding estimated atomic coordinates. Lower dose results in more noise, causing errors in the volume reconstruction, atom identification, and atom classification.

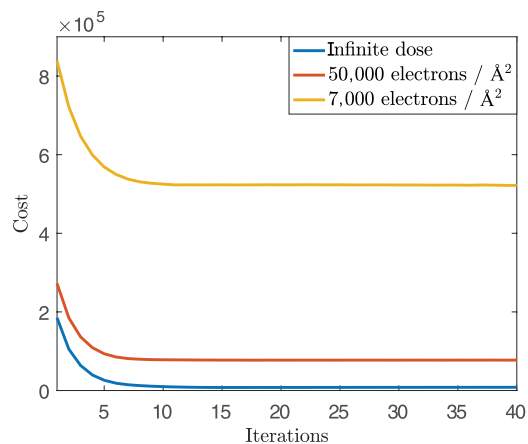


Fig. 5. Cost function vs iterations to show convergence for various dose budgets. Reconstruction becomes noisier as total dose is lowered, and cost function increases. For each reconstruction, we ensure convergence is achieved.

3.3. Effect of missing tilt angles

When the tilt-rotation stage is capable of full-angle tomography, isotropic resolution can be achieved in x , y , and z . However, often projection angles are missing due to sample geometry or stage limitations. This means that the coverage of the object's Fourier spectrum is incomplete [47], often described as a “missing wedge”. In this section, we test our algorithm with missing wedges of 30° and 60° (see Fig. 7(b) and (c), respectively). Across the accessible tilt angles, the angle separation is constant, such that with constant total dose (50,000 electron/ \AA^2) distributed across all acquisitions, the dose per image increases with the size of the missing wedge.

We find that the missing wedge problem primarily impacts axial resolution. As more angles are missed, the axial resolution deteriorates

along the missing wedge direction, increasing errors in atom tracing and identification. Comparing the reconstructions in Fig. 7(a) and (c), the portion of missing sites increases from 0.06% to 0.98%. Not only is it harder to identify atoms, it is also more challenging to correctly identify the 3D positions of each atom. The position error histogram in Fig. 7(c) suggests that position estimate is less accurate in the axial direction as we increase the missing wedge, while the accuracy in the lateral directions are maintained.

3.4. Effect of regularization

Regularization allows us to use prior knowledge about the object to refine the solution space and produce better quality reconstructions, even with noisy data. Because low dose is required in order to preserve sample structure during imaging, our raw data suffers from significant (Poisson-distributed) noise. Here, we examine the effectiveness of three different regularization techniques: pure positivity & real constraint, LASSO regularization, and total variation (TV) regularization, as introduced previously.

The results, shown in Fig. 8, suggest that regularization plays a significant role in denoising with low-dose measurements. With only real & positivity constraints, the background is too noisy to perform accurate atom tracing and the position estimation error is large in all dimensions. The intensity histogram in Fig. 8(a) shows that it also fails to provide two resolved peaks that are needed to perform atom classification.

Both LASSO (Fig. 8(b)) and TV (Fig. 8(c)) regularization significantly improve the quality of the reconstruction. The LASSO reconstruction produces sharp peaks, but shrinks some peak intensities as well as sizes of the potential wells. This leads to a worse distribution of peak intensities, making atomic species classification less accurate. The peak position estimation results are also less accurate for LASSO than TV, as shown in Table 1. Therefore we choose to use TV regularization for our reconstructions.

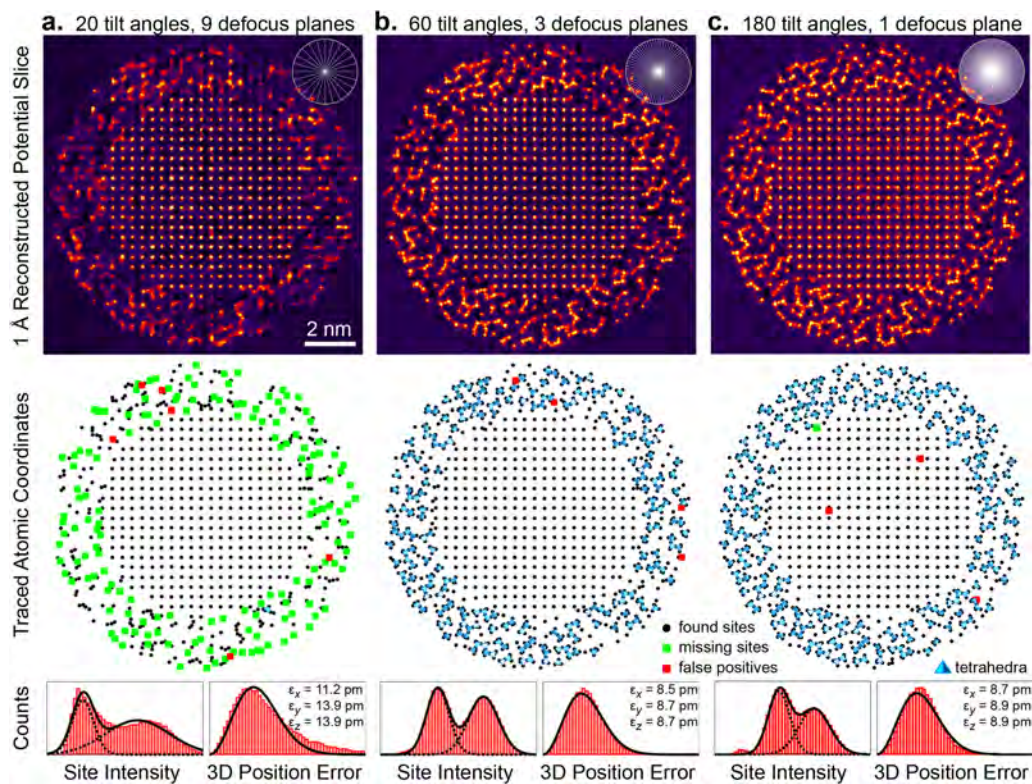


Fig. 6. Varying the number of tilt angles and the number of defocus planes while keeping a constant total dose. Phase contrast AET reconstructions for (a) 20 tilt angles with 9 defocus planes linearly increasing from 20 nm to 100 nm, (b) 60 tilt angles with 3 defocus planes at 20 nm, 45 nm, and 100 nm, and (c) 180 tilt angles with single defocus plane at 100 nm. The case of 3 defocus planes and 60 tilt angles gives minimal error, offering a good trade-off between number of tilt angles and defocus planes.

3.5. Vacancies in crystalline Si and amorphous SiO₂

Our algorithm is capable of identifying single-atom defects or vacancies in the sample. Here, we validate this claim by simulating a Si-SiO₂ tip sample that contains vacancies. We simulate the vacancies and

defects by randomly removing approximately 5% of the atoms in the original sample. Then, with the same geometry and experimental configuration as in Fig. 4(b), we reconstruct the atomic potentials of the defected sample. Fig. 9(a) shows the ground truth atomic potential after the atoms have been removed. The reconstruction result is shown in

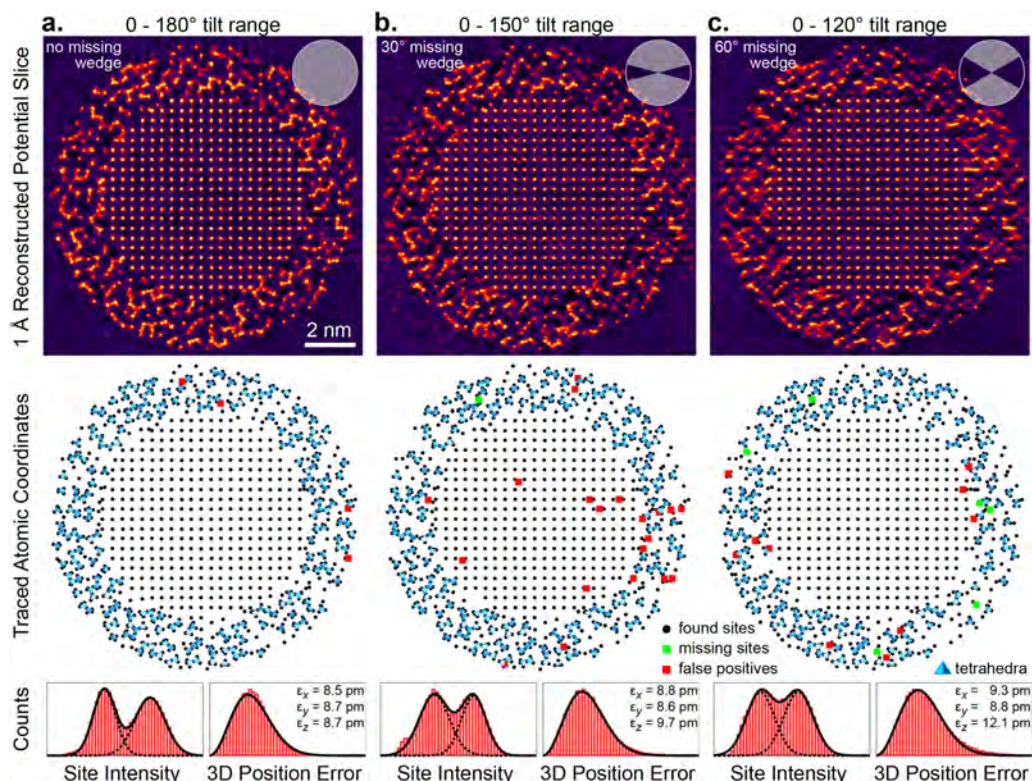


Fig. 7. The missing wedge problem in the measurements primarily affects the axial accuracy of our reconstructions. All scenarios have the same total dose. Phase contrast AET reconstructions for (a) full tomography data with no missing angle, (b) limited tomography data with 30° missing angle, and (c) limited tomography data with 60° missing angle.

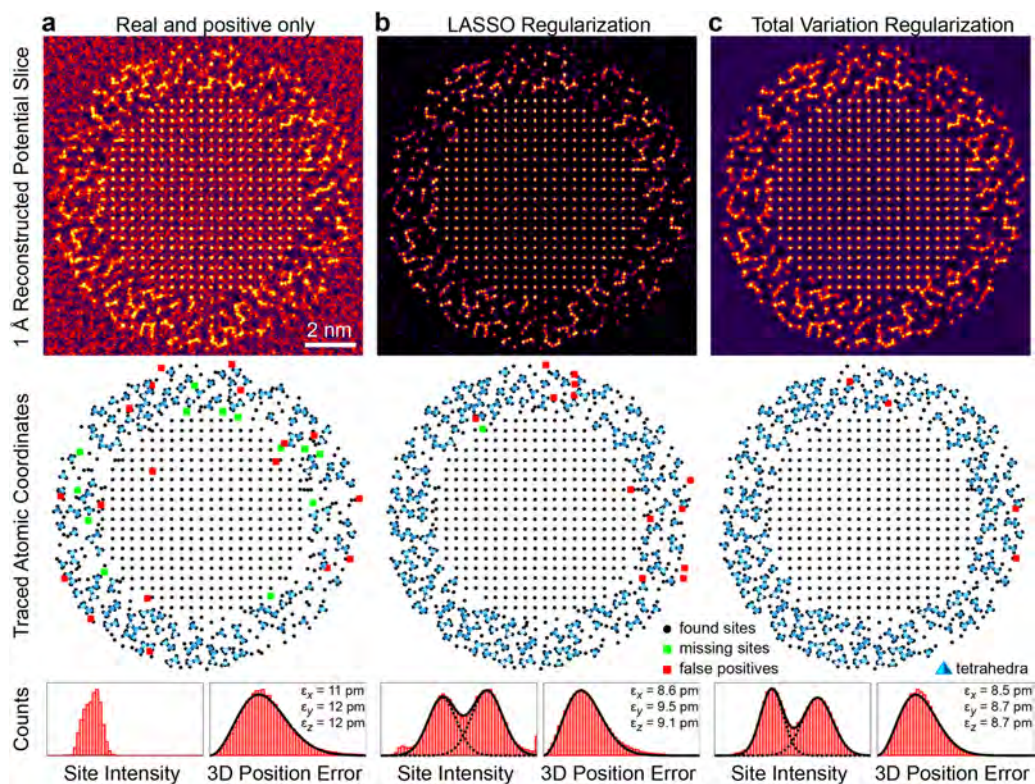


Fig. 8. Regularization is important for image reconstruction quality. Phase contrast AET reconstructions using (a) real & positivity constraints only, (b) LASSO regularization, and (c) total variation (TV) regularization. In this case, TV regularization provides the best performance.

Fig. 9(c). We also refer to Fig. 9(b) for the case where no atoms are removed. Samples can still be reconstructed when there are single-atom defects present, because the algorithm does not assume any structural priors.

3.6. Summary of reconstruction results

Table 1 summarizes all atom tracing and classification results. Note that Figs. 4(b), 6(b), 7(a), and 8(c) are equivalent and are repeated for convenience. We report mean 3D position error, portion of the atoms

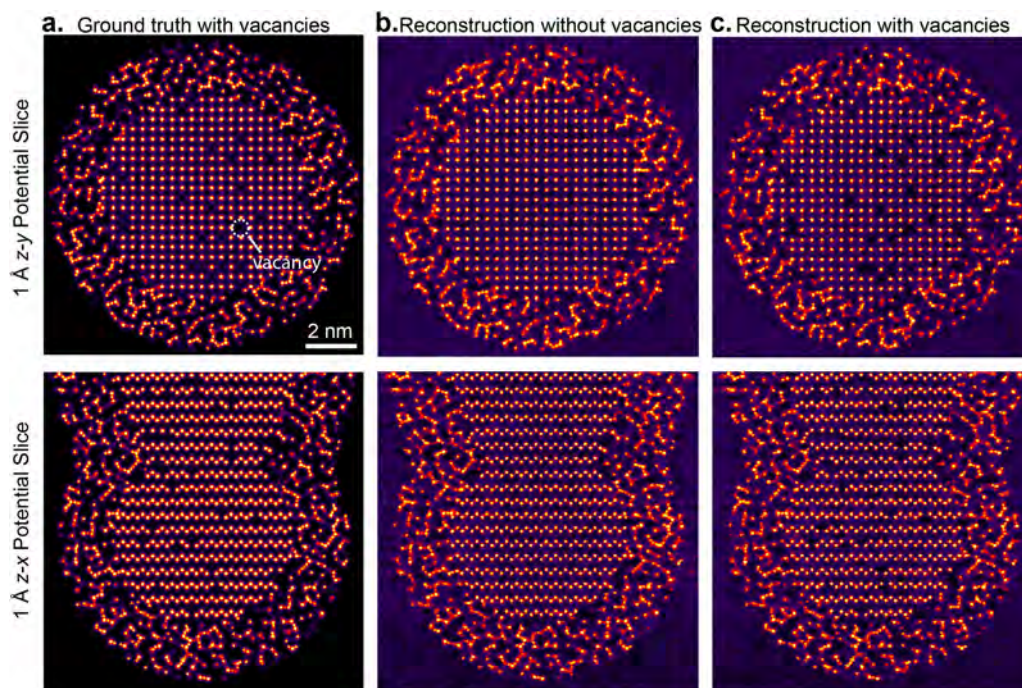


Fig. 9. Phase contrast AET reconstructions with vacancies. (a) Ground truth atomic potential with vacancies. Reconstruction when (b) no vacancies are present, and when (c) 5% of the atoms are removed in the crystalline region and amorphous region. The top row shows slices in $z - y$ direction, and the bottom row shows slices in $z - x$ direction.

Table 1
Summary of atom tracing results, out of 62,402 sites in the tip region with a radius ≤ 12 nm diameter.

Figure(s)	Total dose	N_o	N_f	Tilt span	Regularizer	Position error	Atoms found	False positives	Correct species
4(a)	Infinite	60	3	180°	TV	12.51 pm	99.98%	0.00%	98.63%
4(b)	50,000 electron/Å ²	60	3	180°	TV	13.91 pm	99.94%	0.25%	96.44%
4(c)	7000 electron/Å ²	60	3	180°	TV	21.62 pm	95.24%	9.72%	79.79%
6(a)	50,000 electron/Å ²	20	9	180°	TV	19.11 pm	72.48%	1.26%	82.71%
6(b)	50,000 electron/Å ²	60	3	180°	TV	13.91 pm	99.94%	0.25%	96.44%
6(c)	50,000 electron/Å ²	180	1	180°	TV	14.30 pm	99.97%	0.90%	91.15%
7(a)	50,000 electron/Å ²	60	3	180°	TV	13.91 pm	99.94%	0.25%	96.44%
7(b)	50,000 electron/Å ²	60	3	150°	TV	14.34 pm	99.75%	0.44%	94.67%
7(c)	50,000 electron/Å ²	60	3	120°	TV	15.84 pm	99.02%	2.02%	90.50%
8(a)	50,000 electron/Å ²	60	3	180°	Positive	18.65 pm	97.81%	1.82%	46.81%
8(b)	50,000 electron/Å ²	60	3	180°	Lasso	14.17 pm	99.78%	0.73%	92.53%
8(c)	50,000 electron/Å ²	60	3	180°	TV	13.91 pm	99.94%	0.25%	96.44%
A.10	50,000 electron/Å ²	60	3	180°	TV	10.59 pm	99.95%	1.59%	97.54%

correctly found, portion of false positives, and the portion of atoms where the species are correctly labeled.

4. Conclusion

We have described a reconstruction algorithm for atomic electron tomography, from a tilt series of defocused plane-wave HRTEM images. Our nonlinear model takes into account multiple scattering of the electron beam and uses slice-binning and fast rotation and propagation algorithms to decrease the reconstruction time. We show that TV regularization improves the reconstruction quality. Using a simulated sample with both crystalline Si and amorphous SiO₂ in a core-shell tip geometry, we have demonstrated accurate atomic reconstructions of more than 60,000 atoms in a sample with a diameter up to 12 nm. Our method is robust to low-dose measurements, works for a small number of defocused images and can handle a large missing wedge of tilt angles. Furthermore, we show that our fully coherent model also works with partial coherent data, both temporally and spatially. The end result is atomic-resolution tomographic reconstruction of nanoscale samples containing both strongly and weakly-scattering elements, with either crystalline or amorphous structures. All source codes will be released publicly.

CRediT authorship contribution statement

David Ren: Conceptualization, Formal analysis, Methodology,

Appendix A

A1. Robustness

In this section, we show the robustness of our algorithm by adding several system imperfections that are frequently encountered in real experiments. Then, we use the proposed framework to reconstruct the 3D atomic potentials of the sample. Specifically, based on the tilt and defocus configuration we have shown in Fig. 4(b), we upsample the object and add partially coherent illumination to the measurements.

A1.1. Upsampling

First, we use a voxel size (0.1 Å) finer than the sensor pixel size (0.5 Å) to generate simulated measurements with accurate diffraction effects. For an object of the same volume (24nm)³, this increases the number of voxels from 480³ to 2400³. We then use the multislice model to propagate the electron wave through the finer-grid volume. At the image plane, we bin the pixels to the pixel size of 0.5 Å.

A1.2. Defocus spread

Next, we simulate the effect of chromatic aberration in the electron beam. In particular, we use a Gaussian spread of focal planes for each tilt and defocus to approximate the effect. A defocus spread of 8 Å is reported in [69], so we choose a somewhat larger Gaussian defocus spread of 20 Å with standard deviation of 10 Å. At the image plane, we use Gaussian weighting to incoherently sum the measurements.

A1.3. Spatial coherence

We incorporate spatial partial coherence by simulating a 2D Gaussian spread of input scattering angles for each tilt and defocus. Referring to the work in [33], which reported an angular spread of 200 μrad, we choose a Gaussian angle spread of 400 μrad with standard deviation of 200 μrad. At the image plane, we use a 2D Gaussian weighting to incoherently sum the measurements.

Software, Visualization, Writing - original draft, Writing - review & editing. **Colin Ophus:** Conceptualization, Formal analysis, Methodology, Software, Visualization, Writing - original draft, Writing - review & editing, Project administration, Supervision. **Michael Chen:** Conceptualization, Methodology, Software, Writing - original draft, Writing - review & editing. **Laura Waller:** Conceptualization, Writing - review & editing, Project administration, Supervision.

Declaration of Competing Interest

The authors declare that they do not have any financial or non-financial conflict of interests.

Acknowledgements

We thank Jihan Zhou, Mary Scott, and Hannah DeVyldeere for helpful discussions. This work was supported by STROBE: A National Science Foundation Science & Technology Center under Grant No. DMR 1548924. Work at the Molecular Foundry was supported by the Office of Science, Office of Basic Energy Sciences, of the U.S. Department of Energy under Contract No. DE-AC02-05CH11231. C.O. acknowledges support from the U.S. Department of Energy Early Career Research Program. We also wish to thank the NVIDIA Corporation for donation of GPU resources.

Combining all of the effects above, we simulate a series of measurements, which we then use to reconstruct with the fully-coherent framework outlined in 3. Fig. A.10 shows a reconstructed slice. Despite some reconstruction artifacts, we are able to achieve similar atom identification accuracy comparing with the case in Fig. 4(b), as shown in Table 1. However, clearly the reconstruction artifacts indicated by yellow arrows contribute to the higher false positive rate during atom tracing, so caution should be taken when dealing with real measurements in the future.

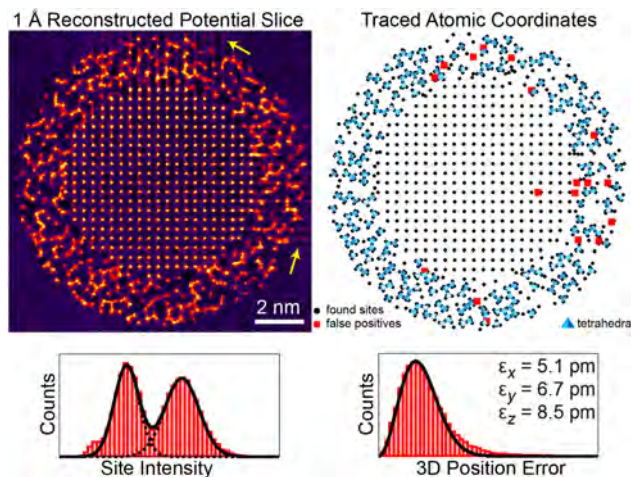


Fig. A1. Phase contrast AET reconstructions for partial coherence with finer sampling during image calculation formalism. Yellow arrows show reconstruction artifacts due to partial coherence.

A2. Heavy atoms

In this section, we demonstrate that the proposed framework can also be generalized to recover the electrostatic potential distribution of samples that contain both light and heavy atoms. Without loss of generality, we replaced the silicon atoms in the previously synthesized sample with Tungsten atoms, which have larger electrostatic potentials, and thus induces stronger dynamical scattering. The sample closely resembles the one demonstrated in [6]. From the sample, we simulated the measurements using the same configuration as that of Fig. 4(b). Fig. A.11 shows the reconstructed potentials of the Tungsten sample.

As shown in Fig. A.11(b), while we recover most of the atoms in the Tungsten tip, the reconstruction quality degrades towards the center of the tip, which corresponds to the thickest region of the needle. These artifacts are due to the large amount of accumulated dynamical scattering. As a result, these artifacts in the reconstruction will contribute to error in future atom localization and identification.

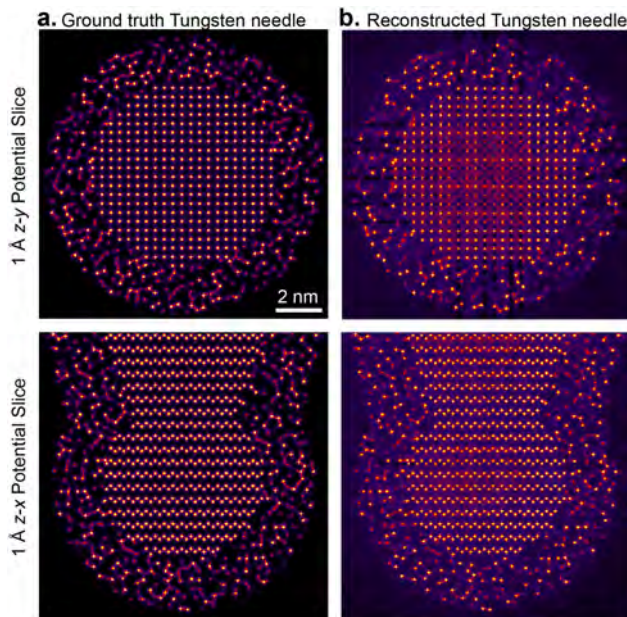


Fig. A2. Phase contrast AET reconstructions for tungsten crystalline and tungsten oxide amorphous structure.

A3. Gradient derivation

In this section, we derive the details of our approach to solve for the inverse problem in vectorized notation. First, we discretize the coordinate system into N_x and N_y pixels for $\mathbf{r} = (x, y)$ respectively. We sample all 2D functions at these discrete coordinates. Then, we raster-scanned the samples

into column vectors in $\mathbb{R}^{N_x N_y}$. In addition, linear operators \mathcal{H} , \mathcal{P} , \mathcal{F} can be represented by matrices \mathbf{H} , \mathbf{P} , $\mathbf{F} \in \mathbb{C}^{N_x N_y \times N_x N_y}$

For a given tilt angle θ_k and defocus f_j measurement, the error function in (5) can be expressed as:

$$e_{k,j}^2 = \mathbf{e}_{k,j}^\dagger \mathbf{e}_{k,j} \quad (\text{A.1})$$

where $\mathbf{e}_{k,j} = \sqrt{\mathbf{I}_{k,j}} - \sqrt{\hat{\mathbf{I}}_{k,j}}$, and $(\cdot)^\dagger$ is the hermitian adjoint of a matrix or a vector. $\mathbf{I}_{k,j}$ is the measured intensity of the image, and $\hat{\mathbf{I}}_{k,j}$ is the estimated intensity through Algorithm 1.

Because the multislice propagation model assumes that the atomic potentials of each layer is independent of each other, we calculate the derivative of $e_{k,j}^2$ with respect to every layer of the potentials \mathbf{W}_m separately by applying the chain rule:

$$\begin{aligned} \nabla_{\mathbf{W}_m} e_{k,j}^2(\mathbf{W}) &= \left[\frac{\partial \mathbf{e}_{k,j}^\dagger \mathbf{e}_{k,j}}{\partial \mathbf{W}_m} \right]^\dagger = \left[\frac{\partial \mathbf{e}_{k,j}^\dagger \mathbf{e}_{k,j}}{\partial \mathbf{e}_{k,j}} \frac{\partial \mathbf{e}_{k,j}}{\partial \mathbf{W}_m} \right]^\dagger \\ &= \left[-2 \mathbf{e}_{k,j} \frac{\partial \mathbf{e}_{k,j}}{\partial \mathbf{W}_m} \right]^\dagger. \end{aligned} \quad (\text{A.2})$$

Next, we show the calculation of $\frac{\partial \mathbf{e}_{k,j}}{\partial \mathbf{W}_m}$ using backpropagation. Following (1) and (3), the derivative of $\mathbf{e}_{k,j}$ with respect to the m^{th} layer \mathbf{W}_m is:

$$\begin{aligned} \frac{\partial \mathbf{e}_{k,j}}{\partial \mathbf{W}_m} &= - \frac{\partial (|\Psi_{\text{exit},k,j}|^2)^{1/2}}{\partial |\Psi_{\text{exit},k,j}|^2} \frac{\partial \text{diag}(\Psi_{\text{exit},k,j}^* \Psi_{\text{exit},k,j})}{\partial \Psi_{N_z+1}} \\ &\quad \frac{\partial \Psi_{N_z+1} \dots \partial \Psi_{m+1} \partial \mathbf{t}_m}{\partial \Psi_{N_z} \partial \mathbf{t}_m \partial \mathbf{W}_m}, \end{aligned} \quad (\text{A.3})$$

where $(\cdot)^*$ denotes complex conjugate, $\text{diag}(\cdot)$ is an operator that puts a vector into the diagonal of a square matrix. Next, we list out the differential terms in the chain rule in (A.3):

$$\frac{\partial (|\Psi_{\text{exit},k,j}|^2)^{1/2}}{\partial (|\Psi_{\text{exit},k,j}|^2)} = \frac{1}{2} \text{diag} \left(\frac{1}{|\Psi_{\text{exit},k,j}|} \right), \quad (\text{A.4})$$

$$\frac{\partial \text{diag}(\Psi_{\text{exit},k,j}^* \Psi_{\text{exit},k,j})}{\partial \Psi_{N_z+1}} = \text{diag}(\Psi_{\text{exit},k,j}^*) \mathbf{H} \mathbf{P}_{\Delta f_j}, \quad (\text{A.5})$$

$$\frac{\partial \Psi_{N_z+1}}{\partial \Psi_{N_z}} = \mathbf{P}_{\Delta z_{N_z}} \text{diag}(\mathbf{t}_{N_z}), \quad (\text{A.6})$$

$$\frac{\partial \Psi_{m+1}}{\partial \mathbf{t}_m} = \mathbf{P}_{\Delta z_m} \text{diag}(\Psi_{N_z}), \text{ and} \quad (\text{A.7})$$

$$\frac{\partial \mathbf{t}_m}{\partial \mathbf{W}_m} = i\sigma \text{diag}(\mathbf{t}_m). \quad (\text{A.8})$$

Combining the terms and apply the complex conjugate operator mentioned in (A.2), we arrive at the gradient of $e_{k,j}^2$ with respect to \mathbf{W}_m :

$$\begin{aligned} \nabla_{\mathbf{W}_m} e_{k,j}^2(\mathbf{W}) &= i\sigma \text{diag}(\mathbf{t}_m^* \Psi_{N_z}^*) \mathbf{P}_{-\Delta z_m} \dots \text{diag}(\mathbf{t}_{N_z}^*) \mathbf{P}_{-\Delta z_{N_z}} \\ &\quad \mathbf{P}_{-\Delta f_j} \mathbf{H}^\dagger \text{diag} \left(\frac{\Psi_{\text{exit},k,j}}{|\Psi_{\text{exit},k,j}|} \right) \left(\sqrt{\hat{\mathbf{I}}_{k,j}} - \sqrt{\mathbf{I}_{k,j}} \right) \end{aligned} \quad (\text{A.9})$$

Notice that computing the gradient is almost equivalent to applying the adjoint operators of the forward propagation to the residual error, hence the name *back propagation*.

If we consider all defocus measurements at tilt angle θ_k , the gradient then becomes:

$$\begin{aligned} \nabla_{\mathbf{W}_m} e_{k,j}^2(\mathbf{W}) &= i\sigma \text{diag}(\mathbf{t}_m^* \Psi_{N_z}^*) \mathbf{P}_{-\Delta z_m} \dots \text{diag}(\mathbf{t}_{N_z}^*) \mathbf{P}_{-\Delta z_{N_z}} \\ &\quad \sum_{j=1}^{N_f} \mathbf{P}_{-\Delta f_j} \mathbf{H}^\dagger \left(\Psi_{\text{exit},k,j} - \text{diag}(\sqrt{\mathbf{I}_{k,j}}) \frac{\Psi_{\text{exit},k,j}}{|\Psi_{\text{exit},k,j}|} \right). \end{aligned} \quad (\text{A.10})$$

Notice that in (A.10), the last term is equivalent to an amplitude substitution as a result of using amplitude-based cost function in (5), and it coincides with the well-known Gerchberg-Saxton type update term [64].

During back propagation, terms such as $\{\psi_m(\mathbf{r})\}_{m=1}^{N_z}$ and \mathbf{W} will be used. However, since they were calculated once in the forward measurement, caching them in the forward propagation is recommended to avoid redundant computation. The specific steps for efficiently computing the gradient are in Algorithms 2 and 3.

A4. Slice-Binning

In both the forward and back propagation, the major bottleneck in computation is the Fourier transform. The number of Fourier transform performed is proportional to the number of slices in z . Since complete tomography without missing angles achieves isotropic resolution, the number of slices in z should match the number of pixels reconstructed in x and y , so the number of slices along the beam direction should be equally as dense, causing very heavy computation.

In this section, we describe our application of the slice-binning in the tomography algorithm [70]. With slice-binning, at every tilt angle we increase the thickness of each slice (i.e. reducing axial resolution per angle). As a result, while total thickness of the sample remains constant, the total number of slices is reduced, along with the computation time. However, because tomography allows us to capture information about each voxel from multiple angles, the redundant information from the other tilt angles allows us to still reconstruct the object at atomic resolution isotropically.

In particular, we sum the 2D projected potentials of N_B consecutive layers at each angle:

$$\mathcal{B}_{N_B}\{V\} = \left\{ \sum_{m=1}^M V_{nN_B+m}(\mathbf{r}) \right\}_{n=0}^{\lceil N_z/N_B \rceil - 1}, \quad (\text{A.11})$$

where $\lceil \cdot \rceil$ is the ceiling function, and

$$M = \begin{cases} N_B & , \text{ if } n < \lceil N_z/N_B \rceil - 1 \\ N_z - nN_B & , \text{ if } n = \lceil N_z/N_B \rceil - 1 \end{cases}. \quad (\text{A.12})$$

We then compute both the forward model and back propagation using this binned potential. After the gradient is calculated, we distribute the gradient to the full volume by applying the adjoint operator, \mathcal{B}^\dagger :

$$\mathcal{B}_{N_B}^\dagger\{V_B\} = \left\{ V_{B, \lfloor \frac{m}{N_B} \rfloor}(\mathbf{r}) \right\}_{m=1}^{N_z}. \quad (\text{A.13})$$

In the simulations shown in the results section, we bin every 10 slices. Since the pixel size in z is 0.5 \AA , the effective slice separation becomes 5 \AA , which is sufficient to recover atomic resolution in the 2D parallel directions. This combined with many tilt angles will produce atomic resolution in 3D with pixel size of $(0.5 \text{ \AA})^3$ (Fig. A.12).

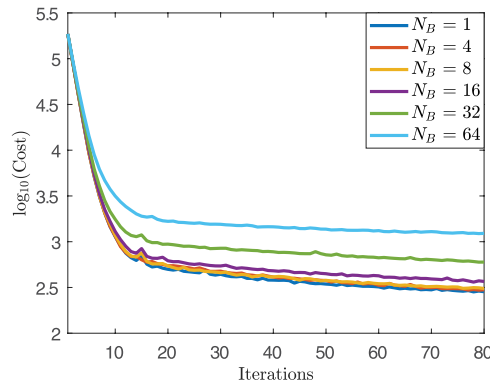


Fig. A3. Plot of cost function vs iterations to show convergence for various binning factors (N_B).

However, the reconstruction quality deteriorates as we gradually increase the number of slices being binned N_B . Therefore, the extent to which we can bin the slices is of special interest. The precise mathematical error analysis is not available due to the non-linearity of the multislice method, and so to estimate an upper bound for slice-binning we use the 3D CTF of the imaging system by assuming single or weakly scattering [41]. Then, we are able to linearize the problem to obtain an estimate of the error. In a traditional imaging system with numerical aperture $NA = \lambda/\Delta x$, where Δx is the pixel size, the axial resolution can be characterized as:

$$\Delta z = \lambda / (1 - \sqrt{1 - NA^2}). \quad (\text{A.14})$$

Based on Nyquist sampling criterion, the maximum thickness for every slice should be less than Δz to support the axial resolution at every angle (Fig. A.13).

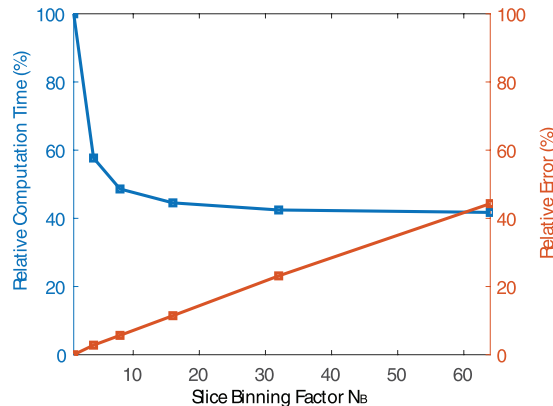


Fig. A4. Plot of relative time savings (left y-axis) and relative error of reconstruction (right y-axis) vs slice binning factors (N_B).

We test the effectiveness and fundamental limit of the proposed slice-binning method. Here, we exponentially increase N_B to examine the effect it has on reconstruction error, computation time, and convergence behavior of the algorithm.

To simplify our discussion, all datasets in the validation process are generated from 60 uniformly separated tilt angles with 3 defocus planes, assuming infinite dose. We do not apply any regularization methods as they alter the convergence behavior depending on the choice of the regularization parameter.

A5. List of symbols

In this second we list all of the symbols defined and used in the article for reader's convenience, shown in Table A.2.

Table A1
List of symbols.

Symbol	Description
Coordinates $\mathbf{q} = (q_x, q_y)$	Frequency coordinates
$\mathbf{r} = (x, y)$	Spatial domain lateral coordinates
z	Spatial domain axial coordinate
Indices	
j	Defocus index
k	Tilt angle index
m	Slice index in axial direction
s	Iteration counter
Constants	Imaginary unit, where $i^2 = -1$
$I_{k,j}$	2D true intensity measurement of k^{th} tilt and j^{th} defocus
N_B	Slice-binning factor
N_f	Number of defocus measurements per tilt
N_s	Number of optimization iterations
N_x, N_y	Number of lateral pixels
N_z	Number of slices in axial direction
N_θ	Number of tilt angles
α	Optimization step size
β	Optimization acceleration factor
τ	Optimization regularization parameter
λ	Electron wavelength
σ	Beam-sample interaction parameter
ψ_0	2D collimated electron beam
Variables $e_{k,j}$	2D residual error between estimated and true measurement of k^{th} tilt and j^{th} defocus
f_j	j^{th} defocus distance
g_m	2D gradient update for W_m
$\hat{I}_{k,j}$	2D estimated intensity measurement of k^{th} tilt and j^{th} defocus
$r_{k,j}$	2D intermediate residual error
$t_m(\cdot)$	2D transmittance function corresponding to W_m
U	3D optimization acceleration momentum
V	3D volume of projected slices
V_m	2D m^{th} projected slice of V
W	Rotated 3D volume of projected slices
W_m	2D m^{th} projected slice of W
θ_k	k^{th} tilt angle
Δz_m	Separation distance between W_m and W_{m+1}
ϕ_m	2D residual error backpropagated to m^{th} layer
ψ_m	2D electron beam forward propagated to m^{th} layer
ψ_{exit}	2D exit wave
Operators $\mathcal{B}\{\cdot\}$	Binning operator (subscript denotes binning factor)
$\mathcal{D}\{\cdot\}$	Finite difference
$\mathcal{F}\{\cdot\}$	Fourier transform
$\mathcal{H}\{\cdot\}$	System transfer function
$\mathcal{P}\{\cdot\}$	Free space propagation (subscript denotes distance)
$\mathcal{R}\{\cdot\}$	Rotation operator (subscript denotes tilt angle)

Data availability: The forward simulation and reconstruction algorithms are implemented in Python, using Arrayfire package for GPU calculations. Atom tracing including position refinement and species determination, as well as visualizations were generated using Matlab codes. The atomic coordinates, reconstructed volumes, and the implementations are available online at <https://github.com/yhren1993/3DPhaseContrastAET>.

Supplementary material

Supplementary material associated with this article can be found, in the online version, at [10.1016/j.ultramic.2019.112860](https://doi.org/10.1016/j.ultramic.2019.112860).

References

- [1] V. Lučić, A. Rigort, W. Baumeister, Cryo-electron tomography: the challenge of doing structural biology in situ, *J. Cell Biol.* 202 (3) (2013) 407–419.
- [2] R. Leary, P.A. Midgley, J.M. Thomas, Recent advances in the application of electron tomography to materials chemistry, *Acc. Chem. Res.* 45 (10) (2012) 1782–1791.
- [3] P.A. Midgley, R.E. Dunin-Borkowski, Electron tomography and holography in materials science, *Nat. Mater.* 8 (4) (2009) 271.
- [4] S. Van Aert, K.J. Batenburg, M.D. Rossell, R. Erni, G. Van Tendeloo, Three-dimensional atomic imaging of crystalline nanoparticles, *Nature* 470 (7334) (2011) 374.
- [5] S. Bals, M. Casavola, M.A. van Huis, S. Van Aert, K.J. Batenburg, G. Van Tendeloo, D. Vanmaekelbergh, Three-dimensional atomic imaging of colloidal core-shell nanoparticles, *Nano Lett.* 11 (8) (2011) 3420–3424.
- [6] R. Xu, C.-C. Chen, L. Wu, M. Scott, W. Theis, C. Ophus, M. Bartels, Y. Yang, H. Ramezani-Dakheel, M.R. Sawaya, et al., Three-dimensional coordinates of individual atoms in materials revealed by electron tomography, *Nat. Mater.* 14 (11) (2015) 1099.
- [7] Y. Yang, C.-C. Chen, M. Scott, C. Ophus, R. Xu, A. Pryor, L. Wu, F. Sun, W. Theis, J. Zhou, et al., Deciphering chemical order/disorder and material properties at the single-atom level, *Nature* 542 (7639) (2017) 75.
- [8] H. Friedrich, M. McCartney, P. Buseck, Comparison of intensity distributions in tomograms from bf tem, adf stem, haadf stem, and calculated tilt series, *Ultramicroscopy* 106 (1) (2005) 18–27.
- [9] A. Pryor, Y. Yang, A. Rana, M. Gallagher-Jones, J. Zhou, Y.H. Lo, G. Melinte, W. Chiu, J.A. Rodriguez, J. Miao, Genfire: A generalized fourier iterative reconstruction algorithm for high-resolution 3d imaging, *Sci. Rep.* 7 (1) (2017) 10409.
- [10] C. Ophus, J. Ciston, J. Pierce, T.R. Harvey, J. Chess, B.J. McMoran, C. Czarnik, H.H. Rose, P. Ercius, Efficient linear phase contrast in scanning transmission electron microscopy with matched illumination and detector interferometry, *Nat. Commun.* 7 (2016) 10719.
- [11] F.-R. Chen, D. Van Dyck, C. Kisielowski, In-line three-dimensional holography of nanocrystalline objects at atomic resolution, *Nat. Commun.* 7 (2016) 10603.
- [12] C. Ophus, J. Ciston, C.T. Nelson, Correcting nonlinear drift distortion of scanning probe and scanning transmission electron microscopies from image pairs with orthogonal scan directions, *Ultramicroscopy* 162 (2016) 1–9.
- [13] K.W. Urban, Studying atomic structures by aberration-corrected transmission electron microscopy, *Science* 321 (5888) (2008) 506–510.
- [14] E.J. Kirkland, *Advanced Computing in Electron Microscopy*, Springer Science & Business Media, 2010.
- [15] C. Jia, S. Mi, J. Barthel, D. Wang, R. Dunin-Borkowski, K. Urban, A. Thust, Determination of the 3d shape of a nanoscale crystal with atomic resolution from a single image, *Nat. Mater.* 13 (11) (2014) 1044.
- [16] G. Argentero, A. Mittelberger, M. Reza Ahmadpour Monazam, Y. Cao, T.J. Pennycook, C. Mangler, C. Kramberger, J. Kotakoski, A. Geim, J.C. Meyer, Unraveling the 3d atomic structure of a suspended graphene/HBN van der Waals heterostructure, *Nano Lett.* 17 (3) (2017) 1409–1416.
- [17] K.H. Downing, R.M. Glaeser, Restoration of weak phase-contrast images recorded with a high degree of defocus: the “twin image” problem associated with CTF correction, *Ultramicroscopy* 108 (9) (2008) 921–928.
- [18] R. Egerton, P. Li, M. Malac, Radiation damage in the TEM and SEM, *Micron* 35 (6) (2004) 399–409.
- [19] G. McMullan, A. Faruqi, D. Clare, R. Henderson, Comparison of optimal performance at 300 keV of three direct electron detectors for use in low dose electron microscopy, *Ultramicroscopy* 147 (2014) 156–163.
- [20] A. Doerr, Single-particle cryo-electron microscopy, *Nat. Methods* 13 (1) (2015) 23.
- [21] J.A. Briggs, Structural biology in situ—the potential of subtomogram averaging, *Curr. Opin. Struct. Biol.* 23 (2) (2013) 261–267.
- [22] T.A. Bharat, C.J. Russo, J. Löwe, L.A. Passmore, S.H. Scheres, Advances in single-particle electron cryomicroscopy structure determination applied to sub-tomogram averaging, *Structure* 23 (9) (2015) 1743–1753.
- [23] M. Vulović, L.M. Voortman, L.J. van Vliet, B. Rieger, When to use the projection assumption and the weak-phase object approximation in phase contrast cryo-em, *Ultramicroscopy* 136 (2014) 61–66.
- [24] C. Ophus, H.I. Rasool, M. Linck, A. Zettl, J. Ciston, Automatic software correction of residual aberrations in reconstructed hrtem exit waves of crystalline samples, *Adv. Struct. Chem. Imag.* 2 (1) (2017) 15.
- [25] M. Gribelyuk, Structure retrieval in HRTEM, *Acta Crystallogr. Sect. A* 47 (6) (1991) 715–723.
- [26] M. Beeching, A. Spargo, A method for crystal potential retrieval in HRTEM, *Ultramicroscopy* 52 (3–4) (1993) 243–247.
- [27] W. Coene, A. Thust, M.O. De Beek, D. Van Dyck, Maximum-likelihood method for focus-variation image reconstruction in high resolution transmission electron microscopy, *Ultramicroscopy* 64 (1–4) (1996) 109–135.
- [28] M. Lentzen, K. Urban, Reconstruction of the projected crystal potential in transmission electron microscopy by means of a maximum-likelihood refinement algorithm, *Acta Crystallogr. Sect. A* 56 (3) (2000) 235–247.
- [29] M. Lentzen, Reconstruction of the projected electrostatic potential in high-resolution transmission electron microscopy including phenomenological absorption, *Ultramicroscopy* 110 (5) (2010) 517–526.
- [30] D. Misell, An examination of an iterative method for the solution of the phase problem in optics and electron optics: I. test calculations, *J. Phys. D* 6 (18) (1973) 2200.
- [31] E.J. Kirkland, Nonlinear high resolution image processing of conventional transmission electron micrographs: I. Theory, *Ultramicroscopy* 9 (1–2) (1982) 45–64.
- [32] L. Allen, M. Oxley, Phase retrieval from series of images obtained by defocus variation, *Opt. Commun.* 199 (1–4) (2001) 65–75.
- [33] L. Allen, W. McBride, N.L. O’Leary, M.P. Oxley, Exit wave reconstruction at atomic resolution, *Ultramicroscopy* 100 (1–2) (2004) 91–104.
- [34] A.M. Maiden, M.J. Humphry, J. Rodenburg, Ptychographic transmission microscopy in three dimensions using a multi-slice approach, *JOSA A* 29 (8) (2012) 1606–1614.
- [35] A. Suzuki, S. Furutaku, K. Shimomura, K. Yamauchi, Y. Kohmura, T. Ishikawa, Y. Takahashi, High-resolution multislice x-ray ptychography of extended thick objects, *Phys. Rev. Lett.* 112 (5) (2014) 053903.
- [36] U.S. Kamilov, I.N. Papadopoulos, M.H. Shoreh, A. Goy, C. Vonesch, M. Unser, D. Psaltis, Learning approach to optical tomography, *Optica* 2 (6) (2015) 517–522.
- [37] L. Waller, L. Tian, Computational imaging: machine learning for 3d microscopy, *Nature* 523 (7561) (2015) 416.
- [38] S. Gao, P. Wang, F. Zhang, G.T. Martinez, P.D. Nellist, X. Pan, A.I. Kirkland, Electron ptychographic microscopy for three-dimensional imaging, *Nat. Commun.* 8 (1) (2017) 163.
- [39] G. Samelsson, Invertible propagator for plane wave illumination of forward-scattering structures, *Appl. Opt.* 56 (14) (2017) 4029–4038.
- [40] P. Li, A. Maiden, Multi-slice ptychographic tomography, *Sci. Rep.* 8 (1) (2018) 2049.
- [41] L. Tian, L. Waller, 3D intensity and phase imaging from light field measurements in an led array microscope, *Optica* 2 (2) (2015) 104–111, <https://doi.org/10.1364/OPTICA.2.000104>.
- [42] J.M. Cowley, A.F. Moodie, The scattering of electrons by atoms and crystals. i. a new theoretical approach, *Acta Crystallogr.* 10 (10) (1957) 609–619.
- [43] W. Van den Broek, C.T. Koch, General framework for quantitative three-dimensional reconstruction from arbitrary detection geometries in TEM, *Phys. Rev. B* 87 (18) (2013) 184108.
- [44] W. Van den Broek, C.T. Koch, Method for retrieval of the three-dimensional object potential by inversion of dynamical electron scattering, *Phys. Rev. Lett.* 109 (24) (2012) 245502.
- [45] X. Jiang, W. Van den Broek, C.T. Koch, Inverse dynamical photon scattering (IDPS): an artificial neural network based algorithm for three-dimensional quantitative imaging in optical microscopy, *Opt. Express* 24 (7) (2016) 7006–7018.
- [46] S.S. Kou, C.J. Sheppard, Image formation in holographic tomography, *Opt. Lett.* 33 (20) (2008) 2362–2364.
- [47] P. Müller, M. Schürmann, J. Guck, *The Theory of Diffraction Tomography*, arXiv:1507.00466, (2015).
- [48] M. Swanwick, P. Keathley, A. Fallahi, P. Krogen, G. Laurent, J. Moses, F. Kärtner, L. Velázquez-García, Nanostructured ultrafast silicon-tip optical field-emitter arrays, *Nano Lett.* 14 (9) (2014) 5035–5043.
- [49] C. Zhu, C.-C. Chen, J. Du, M.R. Sawaya, M. Scott, P. Ercius, J. Ciston, J. Miao, Towards three-dimensional structural determination of amorphous materials at atomic resolution, *Phys. Rev. B* 88 (10) (2013) 100201.
- [50] R. Devine, J. Arndt, Si–o bond-length modification in pressure-densified amorphous SiO₂, *Phys. Rev. B* 35 (17) (1987) 9376.
- [51] M. Haider, S. Uhlemann, E. Schwan, H. Rose, B. Kabius, K. Urban, Electron microscopy image enhanced, *Nature* 392 (6678) (1998) 768.
- [52] P. Batson, N. Dellby, O. Krivanek, Sub-ångström resolution using aberration corrected electron optics, *Nature* 418 (6898) (2002) 617.
- [53] U. Dahmen, R. Erni, V. Radmilovic, C. Kisielowski, M.-D. Rossell, P. Denes, Background, status and future of the transmission electron aberration-corrected microscope project, *Philos. Trans. R. Soc. Lond. A* 367 (1903) (2009) 3795–3808.
- [54] M. Niwa, M. Matsumoto, H. Iwasaki, M. Onada, R. Sinclair, SiO₂/Si interfaces studied by scanning tunneling microscopy and high resolution transmission electron microscopy, *J. Electrochem. Soc.* 139 (3) (1992) 901–906.
- [55] M. Hochella Jr, A. Carim, A reassessment of electron escape depths in silicon and thermally grown silicon dioxide thin films, *Surf. Sci.* 197 (3) (1988) L260–L268.
- [56] F. Krumeich, M. Wark, L. Ren, H.-J. Muhr, R. Nesper, Electron microscopy characterization of silicon dioxide nanotubes, *Z. Anorgan. Allg. Chem.* 630 (7) (2004) 1054–1058.
- [57] Y. He, D.M. Piper, M. Gu, J.J. Travis, S.M. George, S.-H. Lee, A. Genc, L. Pullan, J. Liu, S.X. Mao, et al., In situ transmission electron microscopy probing of native oxide and artificial layers on silicon nanoparticles for lithium ion batteries, *ACS Nano* 8 (11) (2014) 11816–11823.
- [58] A.C. Kak, M. Slaney, *Principles of Computerized Tomographic Imaging*, IEEE Press New York, 1988.
- [59] S.M. Collins, R. Leary, P. Midgley, R. Tovey, M. Benning, C.-B. Schönlieb, P. Rez, M. Treacy, Entropic comparison of atomic-resolution electron tomography of crystals and amorphous materials, *Phys. Rev. Lett.* 119 (16) (2017) 166101.
- [60] M.R. Teague, Deterministic phase retrieval: a Green’s function solution, *JOSA* 73 (11) (1983) 1434–1441.
- [61] Z. Jingshan, R.A. Claus, J. Dauwels, L. Tian, L. Waller, Transport of intensity phase imaging by intensity spectrum fitting of exponentially spaced defocus planes, *Opt. Express* 22 (9) (2014) 10661–10674, <https://doi.org/10.1364/OE.22.010661>.
- [62] A.W. Paeth, A fast algorithm for general raster rotation, *Graphics Interface*, vol. 86, (1986).
- [63] L.-H. Yeh, J. Dong, J. Zhong, L. Tian, M. Chen, G. Tang, M. Soltanolkotabi, L. Waller, Experimental robustness of Fourier ptychography phase retrieval algorithms, *Opt. Express* 23 (26) (2015) 33214–33240, <https://doi.org/10.1364/OE.23.033214>.
- [64] R.W. Gerchberg, Phase determination for image and diffraction plane pictures in the electron microscope, *Optik* 34 (1971) 275.

- [65] N. Parikh, S.P. Boyd, Proximal algorithms, *Found. Trends Optim.* 1 (3) (2014) 127–239.
- [66] L.I. Rudin, S. Osher, E. Fatemi, Nonlinear total variation based noise removal algorithms, *Phys. D* 60 (1–4) (1992) 259–268, [https://doi.org/10.1016/0167-2789\(92\)90242-F](https://doi.org/10.1016/0167-2789(92)90242-F).
- [67] A. Beck, M. Teboulle, Fast gradient-based algorithms for constrained total variation image denoising and deblurring problems, *IEEE Trans. Image Process.* 18 (11) (2009) 2419–2434, <https://doi.org/10.1109/TIP.2009.2028250>.
- [68] D. Kimanius, B.O. Forsberg, S.H. Scheres, E. Lindahl, Accelerated cryo-em structure determination with parallelisation using GPUS in relion-2, *Elife* 5 (2016).
- [69] K. Kimoto, H. Sawada, T. Sasaki, Y. Sato, T. Nagai, M. Ohwada, K. Suenaga, K. Ishizuka, Quantitative evaluation of temporal partial coherence using 3d Fourier transforms of through-focus TEM images, *Ultramicroscopy* 134 (2013) 86–93.
- [70] P.G. Self, M. O'keefe, P. Buseck, A. Spargo, Practical computation of amplitudes and phases in electron diffraction, *Ultramicroscopy* 11 (1) (1983) 35–52.